ADVANCED ENERGY MATERIALS

www.advenergymat.de

Entropy Engineering of SnTe: Multi-Principal-Element Alloying Leading to Ultralow Lattice Thermal Conductivity and State-of-the-Art Thermoelectric Performance

Lipeng Hu, Yang Zhang, Haijun Wu, Junqin Li, Yu Li, Myles Mckenna, Jian He,* Fusheng Liu, Stephen John Pennycook, and Xierong Zeng*

The core effects of high entropy alloys distinguish high entropy alloying from ordinary multielement doping, allowing for a synergy of band structure and microstructure engineering. Here, a systematic synthesis, structural, theoretical, and thermoelectric study of multi-principal-element-alloyed SnTe is reported. Toward high thermoelectric performance, the entropy of mixing needs to be high enough to make good use of the core effects, yet low enough to minimize the degradation of carrier mobility. It is demonstrated that high entropy of mixing extends the solubility limit of Mn while retaining the lattice symmetry, the enhanced Mn content elicits multiscale microstructures. The resulting ultralow lattice thermal conductivity of ≈0.32 W m^{-1} K^{-1} at 900 K in $(Sn_{0.7}Ge_{0.2}Pb_{0.1})_{0.75}Mn_{0.275}Te$ is not only lower than the amorphous limit of SnTe but also comparable to those thermoelectric materials with complex crystal structures and strong anharmonicity. Co-alloying of (Sn,Ge,Pb,Mn) also enhances band convergence and band effective mass, yielding good power factors. Further tuning of the Sn excess yields a state-of-the-art zT ≈1.42 at 900 K in $(Sn_{0.74}Ge_{0.2}Pb_{0.1})_{0.75}Mn_{0.275}Te$. In view of the simple face-centered-cubic structure of SnTe-based alloys, these results attest to the efficacy of entropy engineering toward a new paradigm of high entropy thermoelecrics.

1. Introduction

Heat is ubiquitous: more than two-thirds of the energy we have created is wasted in the form of heat. Thermoelectric (TE) materials can directly convert the untapped waste heat into electricity without rotating parts or greenhouse emissions, hence, TE material research has attracted intense interest over the past few decades.[1] The TE performance of a material is measured by $zT = \sigma S^2 T/\kappa$, where T, σ, S, and κ are the absolute temperature, electrical conductivity, Seebeck coefficient, and total thermal conductivity, respectively. Typically, $\kappa = \kappa_{el} + \kappa_{ph}$, where the κ_{el} and κ_{ph} are the carrier and lattice thermal conductivity, respectively. Since σ, S, and κ_{el} are adversely interrelated whereas the κ_{ph} is relatively independent of σ, S, and κ_{el}, the stride toward high zT is in line with a two-pronged strategy, coined by Slack as "electron-crystal phonon-glass" (ECPG):[2] i) decoupling σ, S, and κ_{el} through band structure engineering toward a high power factor (PF) = σS^2;[3,4] and ii) suppressing the κ_{ph} via all-scale hierarchical microstructures.[5–7] Rooted in the core effects of high entropy alloys (HEAs), entropy engineering enables a synergy of band structure engineering and multiscale hierarchical microstructures through high entropy alloying.

HEAs typically refer to the solid solutions in which more than five principal elements each in 5–35% molar ratio compete for the same crystallographic site, yielding high entropy of mixing and a wider variety of exciting properties.[8] HEA is a subset of multielement-doped materials. Neither the doping process nor the resulting composition would differentiate a

Dr. L. P. Hu, Prof. J. Q. Li, Dr. Y. Li, Prof. F. S. Liu, Prof. X. R. Zeng
College of Materials Science and Engineering
Shenzhen University, and Shenzhen Key Laboratory of Special Functional Materials
Shenzhen 518060, P. R. China
E-mail: junqinli@szu.edu.cn
Dr. L. P. Hu, Prof. X. R. Zeng
Key Laboratory of Optoelectronic Devices and Systems of Ministry of Education and Guangdong Province
College of Optoelectronic Engineering
Shenzhen University
Shenzhen 518060, P. R. China

The ORCID identification number(s) for the author(s) of this article can be found under https://doi.org/10.1002/aenm.201802116.

DOI: 10.1002/aenm.201802116

Y. Zhang, H. J. Wu, Prof. S. J. Pennycook
Department of Materials Science and Engineering
National University of Singapore
7 Engineering Drive 1, Singapore 117575, Singapore
M. Mckenna, Prof. J. He
Department of Physics and Astronomy
Clemson University
Clemson, SC 29634-0978, USA
E-mail: jianhe@g.clemson.edu

HEA from a multielement-doped material, rather, what distinguish (define) a HEA from an ordinary multielement-doped material are the four core effects. Interestingly, these four core effects are inherently pertinent to TE material research:

i) *High-Entropy Effects*: High entropy of mixing tends to form body-centered-cubic (bcc) or face-centered-cubic (fcc) phases, in which high band degeneracy favors a high PF. High entropy of mixing also tends to extend the solubility limits of alloying elements, which in turn expand the phase space for performance optimization.
ii) *Sluggish Diffusion Effects*: Low diffusion kinetics facilitates in situ formation of nanoprecipitates, the key component of all-scale hierarchical microstructures.
iii) *Severe Lattice-Distortion Effects*: Extensive ionic mass and size mismatches help suppress the κ_{ph}.
iv) *The Cocktail Effect*: It refers to those emerging phenomena unexpected from the sum (or the average) of the constituents, which promises a great tunability of HEAs.[8]

The HEA scheme has started to attract interest in TE material research. For example, the configurational entropy was proposed as a performance indicator for TE material prescreening, with the emphases on the Seebeck coefficient and lattice thermal conductivity of equimolar multinary compounds $(Cu/Ag)_2(S/Se/Te)$, $(Cu/Ag)_8Ge(Se/Te)_6$, $(Cu/Ag)(In/Ga)Te_2$, and Mn/Ge/Sn/Pb/Te.[9] $Al_xCoCrFeNi$ was proposed as a potential high-temperature TE material.[10] On one hand, the core effects of HEAs render a natural solution to suppressing the κ_{ph}. A room temperature $\kappa_{ph} \approx 0.6$ W m^{-1} K^{-1} was attained in the simple fcc-structured PbSnTeSe.[11] Fan et al. reported a low $\kappa_{ph} \approx 0.47$ W m^{-1} K^{-1} at 400 K in $BiSbTe_{1.5}Se_{1.5}$.[12] On the other hand, the zT values were not optimized in these cases due to the severely deteriorated carrier mobility. It is a challenge to compensate for the carrier mobility with increasing number of alloying elements.[8]

Instead, we consider the multi-principal-element alloying (MPEA) scheme, a weaker version of the HEA scheme in that the number of alloying elements may be less than five, the compositions are not equimolar, yet the entropy of mixing is high enough to elicit the core effects of HEA. To prove the feasibility of MPEA scheme, the selected material template must be structurally simple enough, chemically tunable enough, yet phase-wise robust enough upon high-entropy alloying. To this end, SnTe is one of the best material templates. SnTe is known as a promising eco-friendly substitute[13] for the classic PbTe TE materials.[3,4] The simple fcc rock salt structure of SnTe makes it easy to showcase the efficacy of MPEA scheme and favors the formation of single phase HEA in view of the high-entropy effects.

Entropy is a performance indicator[9] but high entropy by itself does not suffice high zT. Concerning "what to alloy," we intend to alloy Ge, Pb, and Mn on the Sn site for the following reasons. First of all, in the phase diagram of SnTe–GeTe–PbTe, equimolar ratio of (Sn,Ge,Pb) would not yield a single phase.[14] On the other hand, the equimolar composition $(Sn_{0.25}Ge_{0.25}Pb_{0.25}Mn_{0.25})Te$ forms a single fcc phase due to the high-entropy effects but the PF and zT were less promising.[9] This is the main reason we decided to ease the restriction of equimolar composition and adopted a MPEA approach. Second, it is noted that high Sn content helps stabilize fcc-structured (Sn,Ge,Pb)Te solid solutions.[14] Third, Mn has a high solid solubility up to 13–15 mol% in SnTe, compared to 1 mol% for In and 3 mol% for Cd and Hg.[15–17] Slight excess Mn in $Sn_{1-x}Mn_{1.1x}Te$ helps suppress the formation of $MnTe_2$ secondary phase.[18] Hence, all Mn-containing samples studied in this work adopted nominal compositions $(Sn,Ge,Pb)_{1-x}Mn_{1.1x}Te$ ($x = 0.1$, 0.15, 0.2, 0.25, and 0.3) if not otherwise noted. Last but not the least, to compensate for the degraded carrier mobility in alloys that is detrimental to the PF, we devised a progressive approach: alloying Ge and Pb on the Sn site facilitated band convergence via decreasing the energy difference ΔE between the light- and the heavy-hole band of SnTe,[16] while the same enhanced the Mn solubility via the high-entropy effects, which in turn diminished the ΔE and flattened the valence bands. The intertwined theme of "what to alloy," "how much to alloy," and especially "in what order to alloy" distinguishes this work from most other multielement doping study.

There are more motivations for the present work. Implementing resonant levels,[19] band degeneracy,[15–17,20–23] or band nesting[24–27] schemes in SnTe has resulted in high PF values of ≈20–40 μW cm^{-1} K^{-2}, higher than those of PbTe-based materials.[16,17,20,22,25,26] The interactions between local magnetic moments of Mn and the charge carriers in $Sn_{1.03-x}Mn_xTe$ also led to the enhancement in PF.[17] By contrast, great efforts were exerted to reduce the κ_{ph} below the amorphous limit of SnTe (≈0.5 W m^{-1} K^{-1}) but to no avail.[16,20,28] Accordingly, the present work has two specific objectives: i) attaining a κ_{ph} lower than the amorphous limit of SnTe while retaining a high PF; and ii) reducing the κ_{ph} of the simple fcc-structured SnTe alloys to a level comparable to those ultralow κ_{ph} materials (0.15–0.3 W m^{-1} K^{-1}) with complex crystal structure,[29] intriguing chemical bonds,[30] and strong anharmonicity,[31] e.g., β-Zn_4Sb_3,[29] Cu_2Se,[30] Ag_8GeTe_6,[32] Ag_9GaSe_6,[33] Cu_7PSe_6,[34] MgAgSb,[35] and SnSe.[31]

2. Results and Discussion

Bearing in mind the core effects of HEAs and the two specific objectives, we present the results in three subsections in a row. In Subsection 2.1, the results of phase, structural, theoretical, and TE studies allow us to address the impact of the number of alloying elements on the PF and κ_{ph} in SnTe, (Ge,Sn)Te, (Ge,Pb,Sn)Te, and (Ge,Pb,Mn,Sn)Te. On top of "what to alloy" and "how much to alloy," a new theme "in what order to alloy" emerges. The entropy engineering is realized via combined high-entropy effects, lattice distortion effects, and band convergence scheme. The main theme of Subsection 2.2 is the high Mn content–induced sluggish diffusion effects and multiscale microstructures. The ultralow κ_{ph} of 0.32 W m^{-1} K^{-1} at 900 K in $(Sn_{0.7}Ge_{0.2}Pb_{0.1})_{0.75}Mn_{0.275}Te$ is discussed in relation to the atomic-scale point and line defects, nanoscale strain clusters, and micrometer-scale interfaces. In Subsection 2.3, we further tune the Sn excess to optimize the carrier concentration and thus the PF. A zT of 1.42 at 900 K and high averaged zT values over a wide temperature range are obtained in $(Sn_{0.74}Ge_{0.2}Pb_{0.1})_{0.75}Mn_{0.275}Te$.

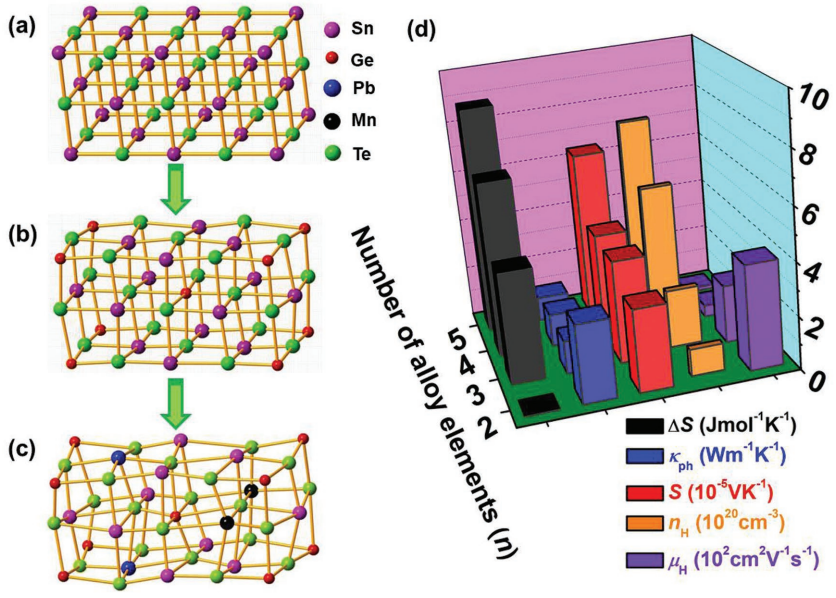

Figure 1. Schematic illustrations of SnTe lattice distortion upon MPEA (not on scale): a) perfect lattice of SnTe, b) lattice distortion caused by Ge dopants, and c) severely distorted lattice caused by Sn–Ge–Pb–Mn coalloying. d) The entropy of mixing ΔS, lattice thermal conductivity κ_{ph}, Seebeck coefficient S, carrier concentration n_H, and carrier mobility μ_H at room temperature of SnTe, $Sn_{0.8}Ge_{0.2}Te$, $Sn_{0.7}Ge_{0.2}Pb_{0.1}Te$, and $(Sn_{0.7}Ge_{0.2}Pb_{0.1})_{0.9}Mn_{0.11}Te$.

2.1. Entropy Engineering via Sn–Ge–Pb–Mn Coalloying

Attaining single-phased HEAs is subject to a subtle entropy–enthalpy balance, which gets harder with increasing number of alloying elements.[8] Despite large entropy of mixing and lattice distortion (**Figure 1**a–c),[9–12] the powder X-ray diffraction (XRD) pattern of (Sn,Ge,Pb,Mn)Te can be indexed to a fcc structure with no discernible secondary phases, the crystal symmetry of SnTe is retained (Figure S1, Supporting Information). These results also corroborate that high entropy of mixing extends the solubility limits of alloying elements. Shown in Figure 1d is the entropy of mixing ΔS, lattice thermal conductivity κ_{ph}, Seebeck coefficient S, carrier concentration n_H, and carrier mobility μ_H at room temperature. According to Boltzmann's hypothesis, the entropy of mixing (ΔS) is given by[9]

$$\Delta S = k_B 1n\Omega = -N_A k_B \sum_{i=1}^{n} x_i 1n x_i, \sum_{i=1}^{n} x_i = 1 \quad (1)$$

where k_B is the Boltzmann constant, Ω is the number of atomic occupation probability, n is the number of the substituted components, x_i is the mole content of the i_{th} component, and N_A is the Avogadro's number. The entropy of mixing for our SnTe-based alloys is substantially enhanced with increasing numbers of alloying elements, which simultaneously results in a reduction in κ_{ph} and an improvement in S.

As expected, the room temperature carrier mobility μ_H is lowered from 395 $cm^2\ V^{-1}\ s^{-1}$ for SnTe to 221 $cm^2\ V^{-1}\ s^{-1}$ for $Sn_{0.8}Ge_{0.2}Te$, and down to 15 $cm^2\ V^{-1}\ s^{-1}$ for $(Sn_{0.7}Ge_{0.2}Pb_{0.1})_{0.9}Mn_{0.11}Te$. The degraded μ_H is a common consequence of high entropy alloying. The reduced μ_H is attributed to the mass fluctuation and strain field; in addition, it is partly due to the increased band effective mass as we will discuss in the following. Concomitant with the deterioration of μ_H is the increment of carrier concentration n_H. Pristine SnTe exhibits a room temperature n_H of 1×10^{20} cm^{-3} in the presence of native Sn vacancies.[16] (Sn,Ge,Pb,Mn) coalloying substantially increases the n_H, similar to the results of Mn,[15,17] Hg,[16] In,[19] Mg,[21] or Cd[26] doping. Theoretical calculations suggested that the variation of n_H is closely tied to the formation energy variation of Sn vacancies regulated by the M^{2+} dopants.[17] Specifically, Ge alloying reduced the bandgap and the high concentration of native Ge vacancy[15] gave rise to an increased n_H; Pb alloying lowered the bandgap despite a lowered formation energy of Sn vacancy,[17] yielding higher n_H.

The impact of MPEA on the electrical conductivity σ is shown in **Figure 2**a. MPEA drastically reduces the magnitude of σ due to the degraded μ_H, despite the increased n_H. The room temperature σ monotonically decreases from 638×10^3 S m^{-1} for pristine SnTe, to 512×10^3 S m^{-1} for $Sn_{0.8}Ge_{0.2}Te$, and further down to 171×10^3 S m^{-1} for $(Sn_{0.7}Ge_{0.2}Pb_{0.1})_{0.9}Mn_{0.11}Te$. Interestingly, the σ of all the samples exhibit power law temperature dependence, and there is a systematic crossover from acoustic phonon scattering to alloy scattering with increasing number of alloying elements. The σ of SnTe displays a $T^{-1.14}$ dependence, consistent with a dominant acoustic phonon scattering ($\sigma \sim T^{-1.5}$). As the number of alloying elements increases, the power law exponent decreases. The $(Sn_{0.7}Ge_{0.2}Pb_{0.1})_{0.9}Mn_{0.11}Te$ alloy exhibits a $\sigma \sim T^{-0.67}$, consistent with a dominant alloy scattering ($\sigma \sim T^{-0.5}$).

The impact of MPEA on the Seebeck coefficient S is depicted in Figure 2b. As shown, the room temperature S increases from 31 μV K^{-1} for SnTe to 39 μV K^{-1} for $Sn_{0.8}Ge_{0.2}Te$, and 64 μV K^{-1} for $(Sn_{0.7}Ge_{0.2}Pb_{0.1})_{0.9}Mn_{0.11}Te$, despite an increased n_H. As shown in Figure 2c, the S values at 600 and 900 K are also enhanced upon the MPEA. To investigate the mechanisms underlying the enhancement of S, we present in Figure 2d the Pisarenko plot, i.e., the S versus n_H. The dotted line is the calculated Pisarenko plot based on a two-valence-band model of SnTe;[19] for comparison, the room temperature S versus n_H for all the samples studied herein, and the literature data of undoped, Bi-, Sb-, In-, Cd-, Hg-, Mg-, Mn-, and Ca-doped SnTe are presented.[16,17,19–21,36] While the results of the undoped and Bi-/Cu-doped samples agree well with the prediction, the In-doped samples exhibit S values higher than the prediction due to resonant levels.[19] Meanwhile, the S can be enhanced by band convergence through Cd, Hg, Mg, Mn, and Ca doping.[15–18,20–22,37] In the band convergence scheme, the energy separation $\Delta E \approx 0.35$ eV between the light and heavy hole band of SnTe is fairly large; reducing the ΔE via doping is restricted by the low solubility of Cd, Hg (≈3 mol%). In this work, such restriction is practically removed by the large solubility of Ge (≈18 mol%), Pb (≈9 mol%), and Mn (≈11 mol%) due to the high-entropy effects. Our Ge-alloyed, Ge–Pb- and Ge–Pb–Mn-coalloyed samples

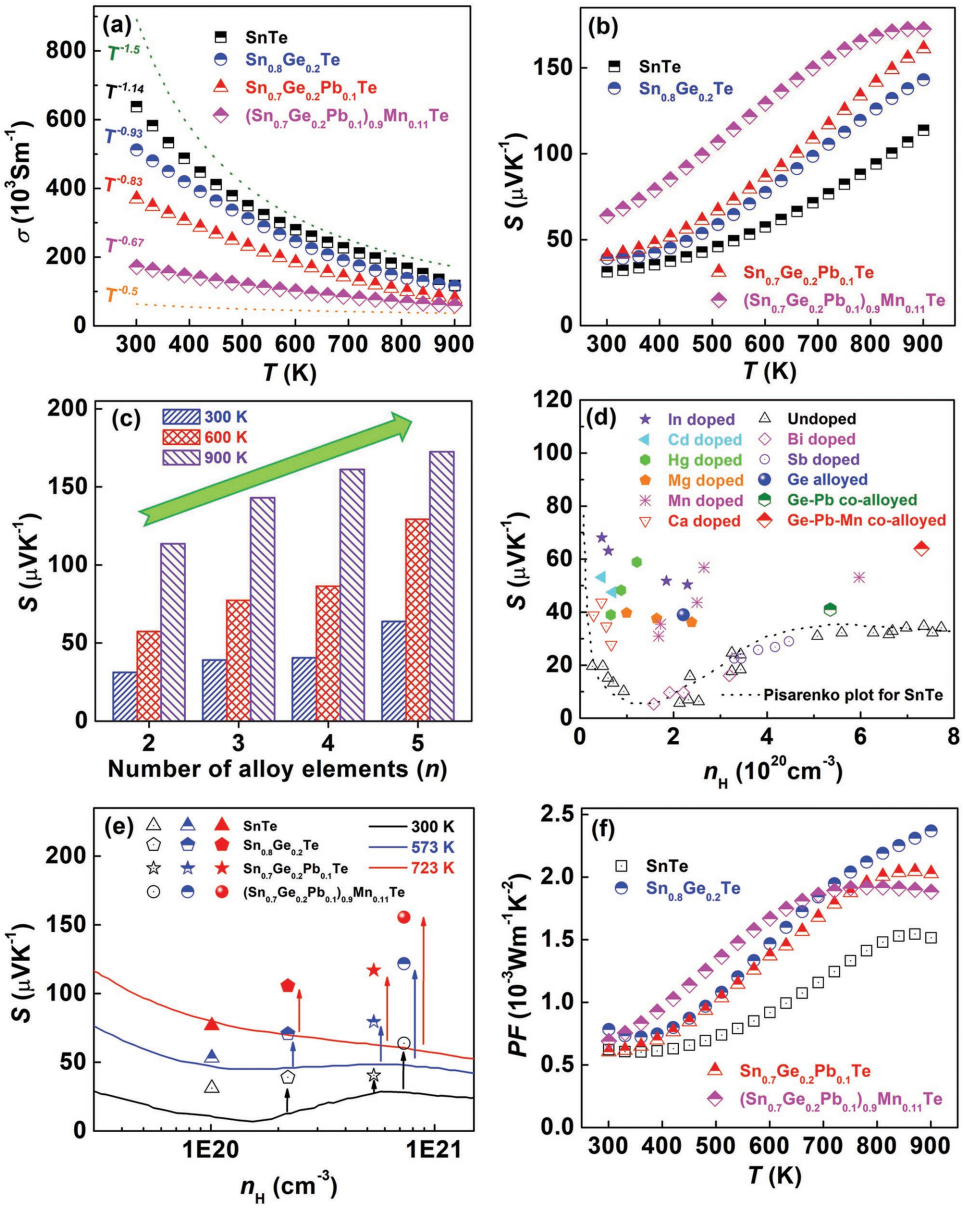

Figure 2. Temperature dependences of a) electrical conductivity, b) Seebeck coefficient, and f) power factor for SnTe, $Sn_{0.8}Ge_{0.2}Te$, $Sn_{0.7}Ge_{0.2}Pb_{0.1}Te$, and $(Sn_{0.7}Ge_{0.2}Pb_{0.1})_{0.9}Mn_{0.11}Te$. c) The impact of MPEA on the Seebeck coefficient at 300, 600, and 900 K. d) Room temperature Seebeck coefficients for the samples studied herein in comparison with literature data;[16,17,19–21,36] the dashed line is the calculated Pisarenko based on a two-valence-band model of SnTe.[19] e) The Seebeck coefficient versus the carrier concentration at 300, 573, and 723 K[38] for the samples studied herein.

exhibit S values larger than the prediction over a wide range of n_H. The room temperature S for our Ge–Pb–Mn-coalloyed sample is as high as the In-doped sample despite an order of magnitude difference in the n_H. Figure 2e displays the S versus n_H at 300, 573, and 723 K.[38] The enhancement of S is more pronounced at higher temperatures, suggesting a better band convergence and/or higher band effective mass.[17]

The substantially enhanced S compensates for the loss of μ_H, yielding improved PFs in the entire temperature range studied (Figure 2f). The maximum PF reaches $\approx 2.4 \times 10^{-3}$ W m^{-1} K^{-2} at 900 K for the $Sn_{0.8}Ge_{0.2}Te$ sample. Further increasing the number of alloy elements, however, leads to lower PF due to the seriously degraded μ_H. Apparently, there is an optimal level of configurational entropy ("window") for the PF. This is a caveat in the entropy engineering of TE materials.

The observed enhancement of S with increasing n_H is somewhat a surprise, which points toward band convergence and/or enhanced band effective mass upon MPEA. To verify, we conducted density functional theory (DFT) calculations and the results are presented in **Figure 3** and Figure S2 (Supporting Information). As shown, the energy separation ΔE is reduced to practically zero for the Ge–Pb–Mn-coalloyed sample, which is the lowest reported ΔE value and thus the best band convergence in IV–VI materials. In addition, both the valence bands become flatter in the Ge–Pb–Mn-coalloyed sample, resulting in substantially increased band effective mass. The large band effective

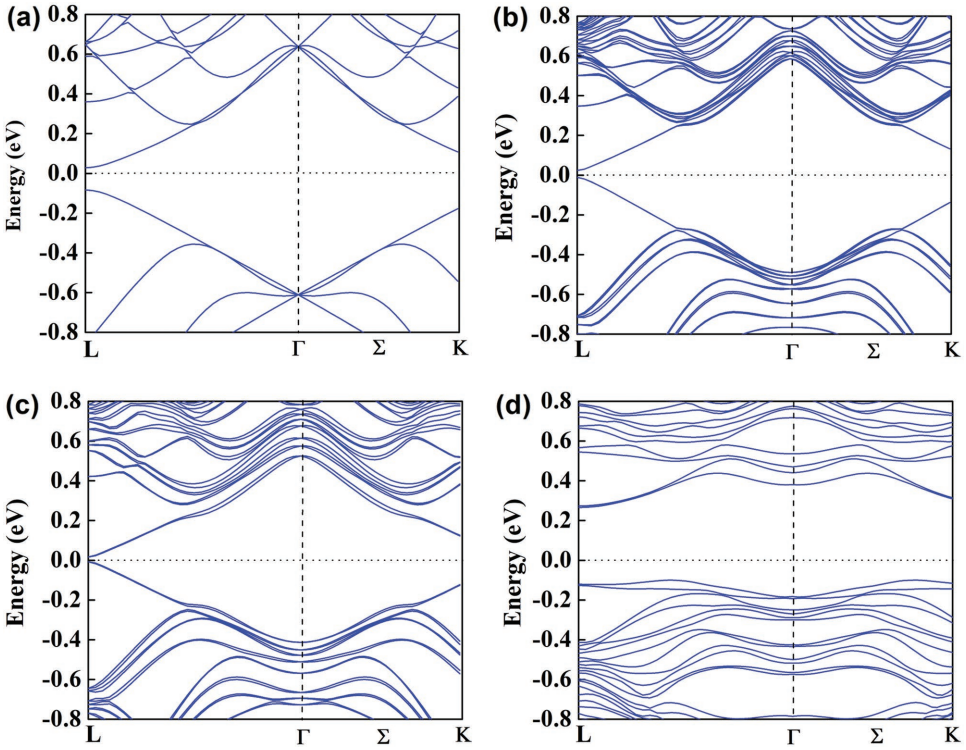

Figure 3. Electron band structures of a) $Sn_{27}Te_{27}$, b) $Sn_{22}Ge_5Te_{27}$, c) $Sn_{19}Ge_5Pb_3Te_{27}$, and d) $Sn_{18}Ge_5Pb_2Mn_2Te_{27}$ supercells in the primitive Brillouin zone (considering the SOC). The energies are shifted with respect to the Fermi energy, which is set to zero. The bandgap exists at the L point and the heavy-hole band at the Σ point in the $3 \times 3 \times 3$ supercell.

mass not only contributes to the enhancement of S but also partly explains the degraded μ_H. Importantly, SnTe is a topological insulator (TI),[39] the band inversion of conduction and valence band in SnTe diminishes the bandgap when alloying with topologically trivial IV–VI isostructurals such as GeTe and PbTe.[40] This is consistent with the results of our DFT calculations (Figure 3). Nonetheless, the bandgap E_g of SnTe is widened upon Sn–Ge–Pb–Mn coalloying, reminiscent of the results in $Sn_{1-x}Mn_xTe$.[15–18,22] While single element doping does not alter the band structure much, the Ge–Pb–Mn coalloying not only reduces the ΔE to nearly zero but also flattens the valence bands, reminiscent of the cocktail effect. Better band convergence and the concomitant flattening of both light and heavy valence bands upon high entropy alloying cannot be achieved by single-element doping.

How to reduce the κ of pristine SnTe that is otherwise too high (7–8 W m^{-1} K^{-1} at 300 K)[16,17] for high zT? Figure 1a–c already provides us with an answer, namely, the MPEA-induced severe lattice distortions. The κ versus T curves for the SnTe-based alloys are plotted in **Figure 4**a. As expected, the room temperature κ is reduced from 7.3 W m^{-1} K^{-1} for binary SnTe to 3.7 W m^{-1} K^{-1} for $Sn_{0.7}Ge_{0.2}Pb_{0.1}Te$, and 2.0 W m^{-1} K^{-1} for $(Sn_{0.7}Ge_{0.2}Pb_{0.1})_{0.9}Mn_{0.11}Te$. To estimate the κ_{el}, we use the Wiedemann–Franz relation $\kappa_{el} = L\sigma T$, where the Lorenz number L was estimated using the formula $L = 1.5 + \exp(-|S|/116)$.[41] As multi-principal-element alloying degrades the σ, the κ_{el} is reduced accordingly (Figure S3, Supporting Information).

The κ_{ph} of all samples, calculated by subtracting the κ_{el} from the κ, are plotted as a function of T in Figure 4b. Without noticeable nanoprecipitates, the MPEA-induced severe lattice distortions alone remarkably suppress the κ_{ph}. With increasing number of alloying elements, the κ_{ph} is monotonically reduced in the entire temperature range studied (Figure 4c). Specifically, the room temperature κ_{ph} is reduced from 3.0 W m^{-1} K^{-1} for pristine SnTe to 1.2 W m^{-1} K^{-1} for $Sn_{0.8}Ge_{0.2}Te$, and further down to 0.9 W m^{-1} K^{-1} for $(Sn_{0.7}Ge_{0.2}Pb_{0.1})_{0.9}Mn_{0.11}Te$. The minimum κ_{ph} for Ge–Pb–Mn-coalloyed sample is 0.55 W m^{-1} K^{-1}, not only lower than that of most iv–vi solid solutions (Figure 4d)[19,37,42,43] but also comparable to the amorphous limit of SnTe (0.5 W m^{-1} K^{-1}). In particular, the κ_{ph} exhibits power law behavior: the power law exponent of κ_{ph} reduces from –0.96 for SnTe to –0.61 for $(Sn_{0.7}Ge_{0.2}Pb_{0.1})_{0.9}Mn_{0.11}Te$, similar to the trend of σ. The observed variation of temperature dependence of κ_{ph} is attributed to a systematic crossover from Umklapp scattering of acoustic phonons with T^{-1} dependence to alloy scattering with $T^{-0.5}$ dependence with increasing number of alloying elements.

The inflexion in the κ_{ph} versus T for SnTe near 800–900 K (Figure 4b) is an indicator of the bipolar effect.[16] Widening the E_g and increasing the majority carrier concentration are two effective ways to suppress the detrimental bipolar effect.[17] In fact, Sn–Ge–Pb–Mn coalloying has accomplished both in a synergetic manner in light of the cocktail effect. The n_H is remarkably increased with the (Sn,Ge,Pb,Mn) coalloying, shifting the Fermi level deeper into the valence band. Meanwhile, the E_g of SnTe is enlarged through alloying with MnTe that has a larger bandgap (0.74 eV),[17] as corroborated by the results of our DFT calculations (Figure 3).

The temperature-dependent zT values for all the samples are presented in Figure 4e. The zT monotonically increases with

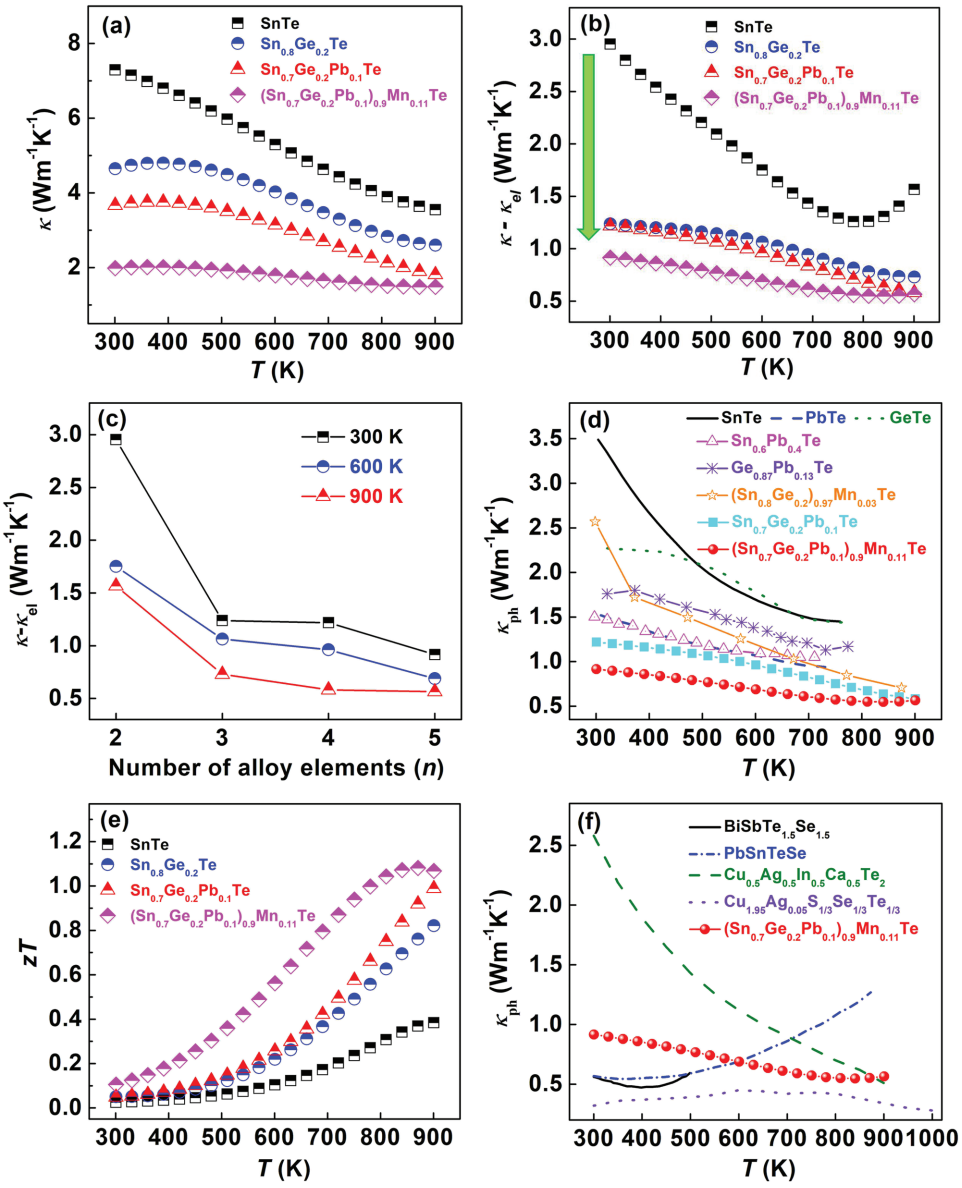

Figure 4. Temperature dependence of a) total thermal conductivity, b) lattice thermal conductivity, and e) zT for the SnTe-based alloys. c) The κ_{ph} at 300, 600, and 900 K as a function of the number of alloying elements. The κ_{ph} for the $(Sn_{0.7}Ge_{0.2}Pb_{0.1})_{0.9}Mn_{0.11}Te$ sample in comparison with literature data of d) several iv–vi solid solutions,[19,37,42,43] and f) several high-entropy TE materials.[9,11,12]

increasing temperatures for all the samples. With increasing number of alloy elements, the peak zT is substantially enhanced from 0.38 for SnTe to 0.82 for $Sn_{0.8}Ge_{0.2}Te$, and further to 1.07 for $(Sn_{0.7}Ge_{0.2}Pb_{0.1})_{0.9}Mn_{0.11}Te$. The efficacy of MPEA in SnTe is thus proved. In the following section, our main focus will be shifted to all-scale hierarchical microstructures and the further reduction of κ_{ph}.

2.2. All-Scale Hierarchical Microstructures via Mn Alloying

The κ_{ph} values derived in Section 2.1 are still higher than those of typical HEAs with equimolar compositions (Figure 4f).[9,11,12] These κ_{ph} values are derived by the severe lattice distortion effects but in absence of nanoprecipitates. As a key component of hierarchical microstructures, nanoprecipitates are formed by the sluggish diffusion effects in HEAs. To enhance sluggish diffusion effects, we increase the Mn ratio toward its solubility limit.

It should be noted that the all-scale hierarchical microstructures derived in this work may somewhat resemble those low entropy TE materials but they differ in important aspects. First, it is the core effects of HEAs that allowed for enhanced Mn solubility that in turn elicited such rich microstructures. Second, strain clusters and intertwined line defect dislocation arrays are for the first time reported in HEAs.

Figure 5a depicts the powder XRD patterns for the $(Sn_{0.7}Ge_{0.2}Pb_{0.1})_{1-x}Mn_{1.1x}Te$ samples ($0.1 \le x \le 0.3$). Again,

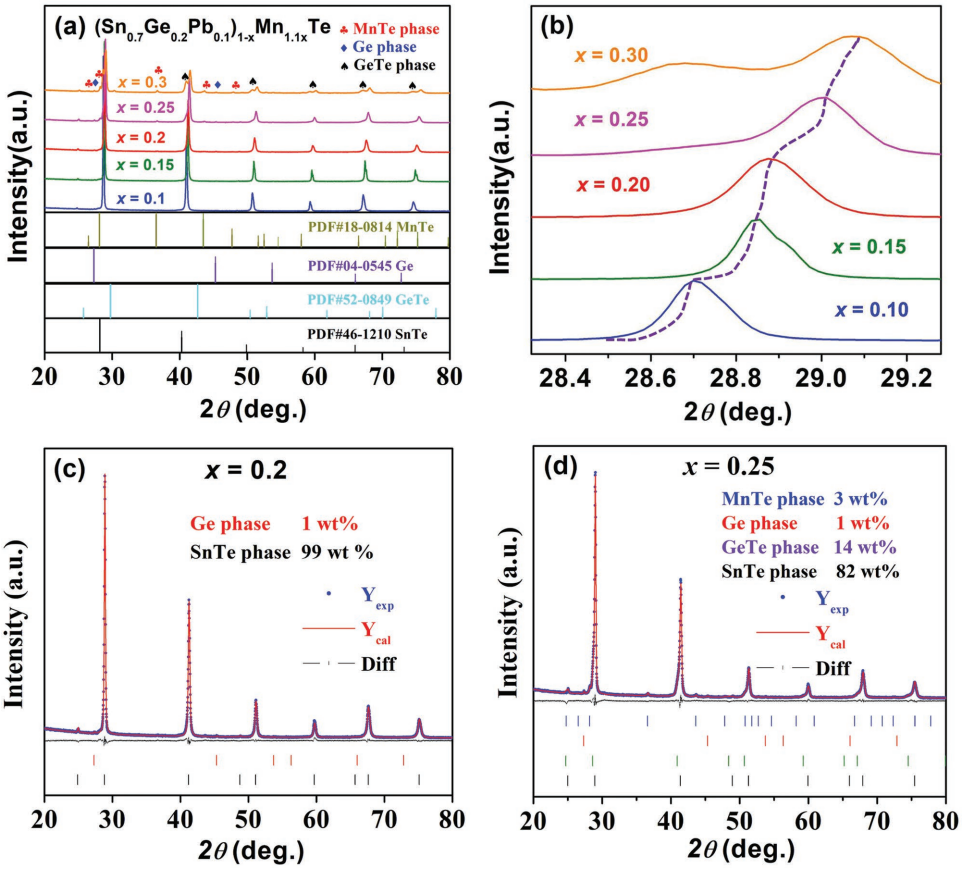

Figure 5. a) Powder XRD patterns and b) an enlarged view of (200) Bragg peaks for the $(Sn_{0.7}Ge_{0.2}Pb_{0.1})_{1-x}Mn_{1.1x}Te$ samples (x = 0.1–0.3). Rietveld refinement results of the $(Sn_{0.7}Ge_{0.2}Pb_{0.1})_{1-x}Mn_{1.1x}Te$ samples with c) x = 0.2 and d) x = 0.25.

all Bragg reflections are well indexed to a fcc-structured SnTe with no discernible secondary phases at $x < 0.2$. As shown in Figure 5b, the (200) diffraction peak shifts to higher angles with increasing Mn content, consistent with a smaller radius of Mn compared to the average radius of Sn, Ge, and Pb. The solubility limit of Mn in SnTe is known to be ≈13–15 mol%.[15–18] Hence, a higher solubility limit of Mn of ≈20 mol% found in $(Sn_{0.7}Ge_{0.2}Pb_{0.1})_{1-x}Mn_{1.1x}Te$ attests to the fact that the high-entropy effect tends to expand the solubility limits of Mn.[8] High solubility of Mn yields a multitude of atomic-scale point defects that would effectively scatter short-wavelength phonons at elevated temperature.

At a Mn content x = 0.2, however, Ge secondary phase is identified. GeTe and MnTe secondary phases are observed when $x > 0.25$. Phase analysis by the Rietveld refinement (Figure 5c,d) indicates that the x = 0.2 sample contains 99 wt% of SnTe-based solid solution and 1 wt% of Ge phase, while the x = 0.25 sample consists of a SnTe-based solid solution (82 wt%), GeTe phase (14 wt%), MnTe phase (3 wt%), and Ge phase (1 wt%). Furthermore, we performed scanning electron microscopy (SEM)/energy dispersive X-ray spectroscopy (EDS) measurements to characterize the micromorphology of the x = 0.25 sample (Figure S4, Supporting Information), the results of which show the presence of multiple precipitates, which lead to a multitude of interfaces at micrometer scale that effectively scatter long wavelength phonons.

The x = 0.25 sample was subject to more detailed micromorphology analysis using scanning transmission electron microscopy (STEM)/transmission electron microscopy (TEM) because of its rich phases/microstructures. **Figure 6**a is a STEM high angle angular dark field (HAADF) image with a *Z*-contrast feature,[44] showing several sub-μm MnTe laminates. The elemental distribution from EDS mappings (Figure 6b1–b5) confirms the laminates are indeed MnTe. Figure 6c1 is a high-resolution TEM (HRTEM) image focusing on the phase boundary between the MnTe laminates and SnTe host matrix. The periodically arrayed structural modulation at the phase boundary arises from the lattice mismatch between MnTe and SnTe, which yields a periodic array of dislocation cores.[45] Such a phase-contrast feature is weaker in the STEM-annular bright-field (ABF) imaging mode (Figure 6c2), and is absent in the STEM-HAADF imaging mode with insignificant phase contrast contribution (Figure 6c3). The fast Fourier transformation (FFT) images (the insets in Figure 6c1–c3) show centrosymmetric peak splitting, reflecting not only the lattice difference but also the lattice alignment between MnTe precipitates and the SnTe host matrix. Geometric phase analysis (GPA) was employed to analyze the possible strain near the phase boundary.[46] The periodic high-strain arrays shown in Figure 6d2,d3,e1 are consistent with the structure modulation with arrays of dislocations cores at the phase boundary. The precipitates also show a high density of disordered strain cores, reflecting that the

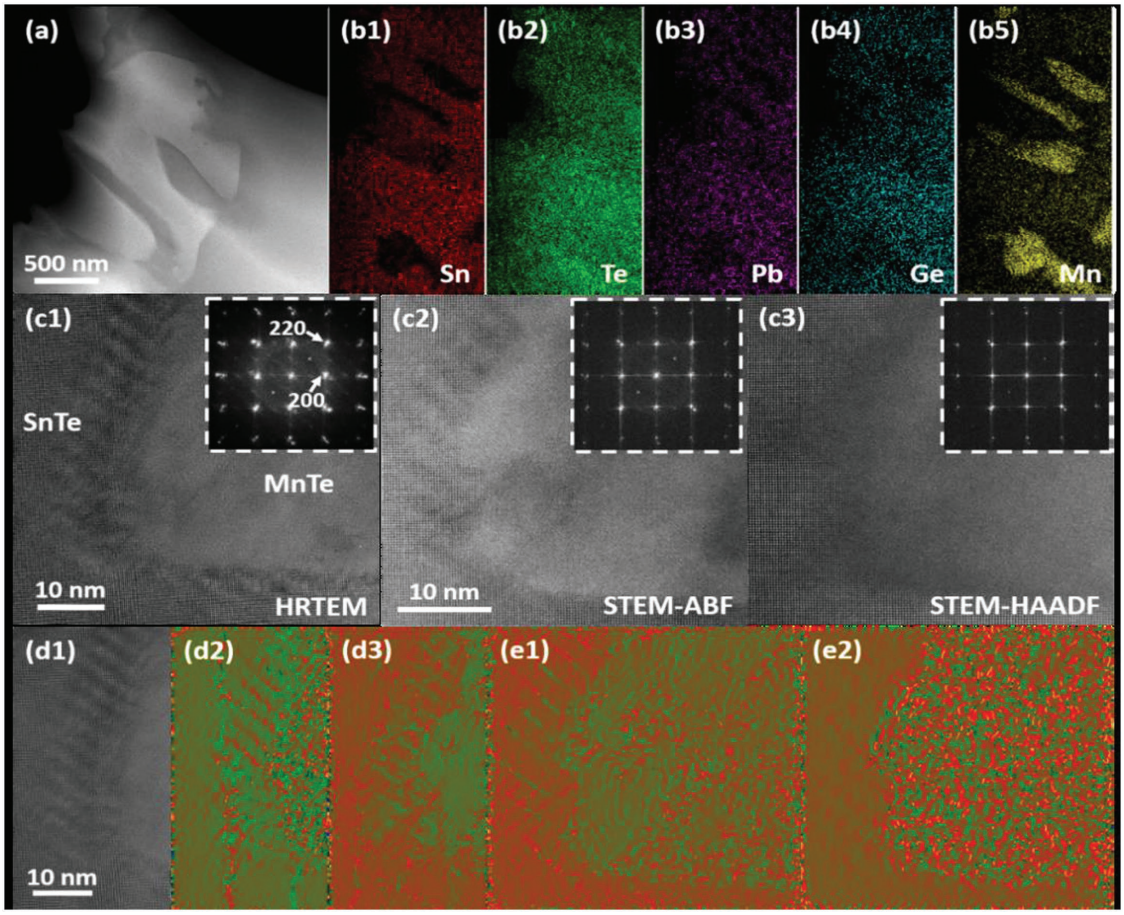

Figure 6. Sub-micrometer micromorphology of MnTe precipitates. a) STEM-HAADF image showing several sub-micrometer scale MnTe precipitates. b1–b5) STEM-EDS elemental mappings of Sn, Te, Pb, Ge, and Mn, respectively. c1–c3) HRTEM, STEM-ABF, and STEM-HAADF image focusing on the boundary between MnTe precipitate and SnTe matrix. Insets are respective FFT images. d1) Enlarged HRTEM image of the phase boundary and d2,d3) its GPA results of 200 and 220 reflection spots. e1,e2) GPA results of (c2) from 220 and 200 reflection spots.

precipitates are also highly distorted due to the (Sn,Ge,Pb,Mn) coalloying.

Figure 7 shows three types of strain networks: line defects, nanoscale strain clusters, and dislocation arrays. Figure 7a1–a3 are low-magnification TEM, STEM-ABF, and STEM-HAADF images roughly from the same area showing a high density of line defects and nanoscale strain clusters. Figure 7b shows a long array of dislocation cores and several line defects. The HRTEM image in Figure 7c focuses on two parallel line defects, and the length direction is along (110). GPA was also performed to analyze the strain near a line defect (Figure 7d), and the result shows that high-strain dislocation cores segregate along the line defect (Figure 7f1–f4). As shown in Figure 7a1–a3, the strain clusters are always at the intersections of line defects. One strain cluster is shown in Figure 7g. Different from the line defect (Figure 7e), the electron reflection of the strain cluster shows clear ½(200) and ½(220) superlattices.[44] The GPA analysis points toward a high density of high-strain dislocation cores insides the strain cluster. The combined effect of these high-strain defects at various scales greatly contributes to the scattering of short- and mid-wavelength phonons. Notably, the intertwined line defects, nanoscale strain clusters, and dislocation arrays observed in (Ge,Pb,Mn,Sn)Te were not reported in any single Ge-/Pb-/Mn-doped SnTe.

As expected, the all-scale hierarchical microstructures also have a direct impact on the electrical transport. As displayed in **Figure 8**a, the μ_H falls from 15 to 5 $cm^2\ V^{-1}\ s^{-1}$ with the x value increasing from 0.1 to 0.3, likely due to the atomic-scale point and line defects, nanoscale strain clusters, and micrometer-scale interfaces. The μ_H of our (Sn,Ge,Pb,Mn)Te sample at high Mn content comes quite close to the ones reported in other (Sn,Mn)Te,[15–17,27] though they exhibit very different values at the low Mn content. In addition, Mn is an effective acceptor, a higher solubility of ≈20 mol% Mn allows for a higher n_H (Figure 8b): the n_H for the $x = 0.3$ sample reaches $9.9 \times 10^{20}\ cm^{-3}$, which is one of the highest reported n_H values of SnTe-based alloys.

The σ of the $(Sn_{0.7}Ge_{0.2}Pb_{0.1})_{1-x}Mn_{1.1x}Te$ samples are depicted in Figure 8c. The increase of the Mn content x from 0.1 to 0.3 gives rise to a monotonical drop in σ due to the dramatically diminished μ_H. Figure 8d presents the temperature-dependent S of all the samples. The magnitude of S increases with increasing x values. Specifically, the room temperature S value increases from 64 $\mu V\ K^{-1}$ for the $x = 0.1$ sample to 82 $\mu V\ K^{-1}$ for the $x = 0.3$ sample.

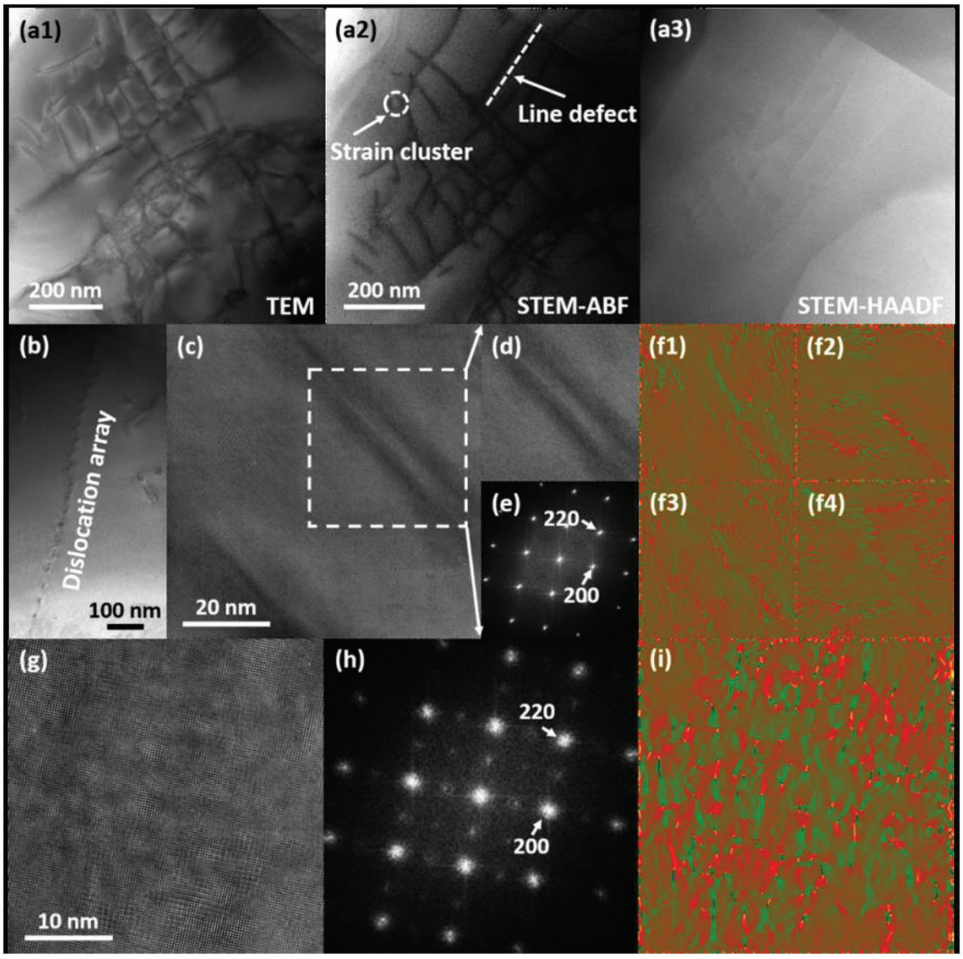

Figure 7. Structure of line defects and nanoscale strain clusters. a1–a3) Low-magnification TEM, STEM-ABF, and STEM-HAADF images showing a high density of line defects. b) TEM image of dislocation arrays. c) HRTEM image of two line defects. d) Enlarged image from (c). e) FFT image of (d). f1–f4) GPA results from two {100} and two {110} reflection spots. g) HRTEM image of one nanoscale strain cluster. h) FFT image of (g) showing ½(200) and ½(220) superlattices. i) GPA result from ½(200) superlattices.

The Pisarenko plot of S versus n_H at room temperature can be clearly divided into three regimes: regime I dominated by the light valence band, regime II dominated by the light valence band and partially heavy valence band, and regime III dominated by both light and heavy valence bands (Figure 8e). It can be readily seen that most Mn-alloyed SnTe locate in regimes I and II, e.g., a S of 91 μV K^{-1} at 300 K was reported by Wang et al.[27] at a low $n_H \approx 1.5 \times 10^{19}$ cm^{-3}. By contrast, all our $(Sn_{0.7}Ge_{0.2}Pb_{0.1})_{1-x}Mn_{1.1x}Te$ samples lie in regime III, a S of 82 μV K^{-1} at $n_H \approx 9.9 \times 10^{20}$ cm^{-3}. Similar high S at a carrier concentration two orders of magnitude higher is ascribed to a combination of better band convergence and larger band effective mass induced by higher solubility of Mn (≈20 mol%). Compared to the literature data of Mn-doped SnTe, our Ge–Pb–Mn-coalloyed SnTe samples tend to have lower S values at high temperatures, likely due to the n_H that is too high.[15–17,22] In Figure 8f, we plot the PF as a function of T. The PF mildly decreases to some degree with increasing Mn content. The PF value at 900 K is 1.76×10^{-3} W m^{-1} K^{-1} for the $x = 0.1$ sample, and it slightly reduces to 1.65×10^{-3} W m^{-1} K^{-1} for the $x = 0.25$ sample.

Figure 9a depicts the temperature dependence of κ for all the samples. The κ initially dramatically falls ($0.1 < x < 0.25$) and then slightly rises ($x > 0.25$) with increasing Mn content. Specifically, the room temperature κ drops from 1.98 W m^{-1} K^{-1} for the $x = 0.1$ sample to 1.39 W m^{-1} K^{-1} for the $x = 0.25$ sample, and slightly increases to 1.43 W m^{-1} K^{-1} for the $x = 0.3$ sample. The κ_{el} shows a systematic reduction with increasing x values (Figure S5, Supporting Information). The temperature variation of κ_{ph} is displayed in Figure 9b. The κ_{ph} also exhibits a trend of initial drop and subsequently slight increase with increasing x values, similar to what is observed for κ. A typical room temperature κ_{ph} of 0.92 W m^{-1} K^{-1} is observed for the $x = 0.1$ sample, which first decreases to 0.81 W m^{-1} K^{-1} for the $x = 0.25$ sample, and then to 0.93 W m^{-1} K^{-1} for the $x = 0.3$ sample. A similar trend is found at 600 and 900 K (Figure 9c). In particular, the minimum κ_{ph} is only 0.32 W m^{-1} K^{-1} at 900 K for the $x = 0.25$ sample, compared to 0.55 W m^{-1} K^{-1} for the $x = 0.1$ one. As mentioned above, the $x = 0.25$ sample exhibits all-scale hierarchical microstructures including atomic-scale point and line defects, nanoscale strain clusters, and micrometer-scale interfaces that can effectively scatter a wide spectrum of heat-carrying phonons.

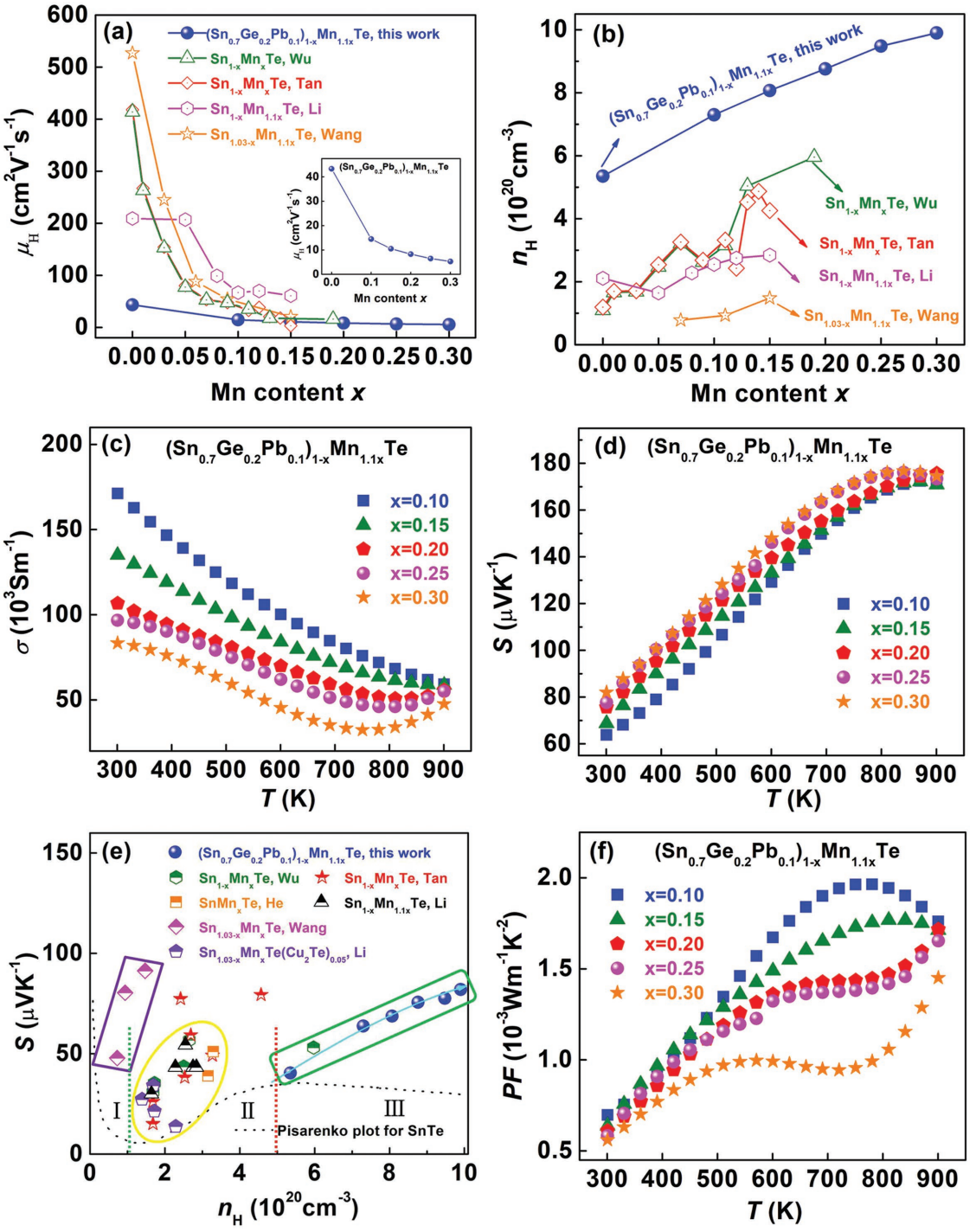

Figure 8. Room temperature a) hole mobility and b) hole concentration as a function of Mn ratio for the $(Sn_{0.7}Ge_{0.2}Pb_{0.1})_{1-x}Mn_{1.1x}Te$ series, in comparison with other Mn-doped SnTe alloys.[15,16,18,27] Temperature dependence of c) electrical conductivity, d) Seebeck coefficient, and f) power factor for $(Sn_{0.7}Ge_{0.2}Pb_{0.1})_{1-x}Mn_{1.1x}Te$. e) Room temperature Pisarenko plot for $(Sn_{0.7}Ge_{0.2}Pb_{0.1})_{1-x}Mn_{1.1x}Te$ in comparison with the literature data of other Mn-doped SnTe alloys.[15–18,22,27]

Considering the two specific objectives of the present work, the observed ultralow κ_{ph} is not only a minimum compared to literature data of SnTe-based alloys (Figure 9d),[15–17,19–21,24,26,28,47,48] but also is lower than that of classic TE materials such as Bi_2Te_3,[49] PbTe,[6] and $CoSb_3$[7] (Figure 9e). Furthermore, this value is close to those state-of -the-art TE materials with intrinsic low κ_{ph},[29–35,50] thereby confirming the efficacy of entropy engineering. Finally, the hump in κ_{ph} for the $x = 0.3$ sample, which is absent from other samples, is attributed to the substantial presence of MnTe.[17] As illustrated in Figure 9f,

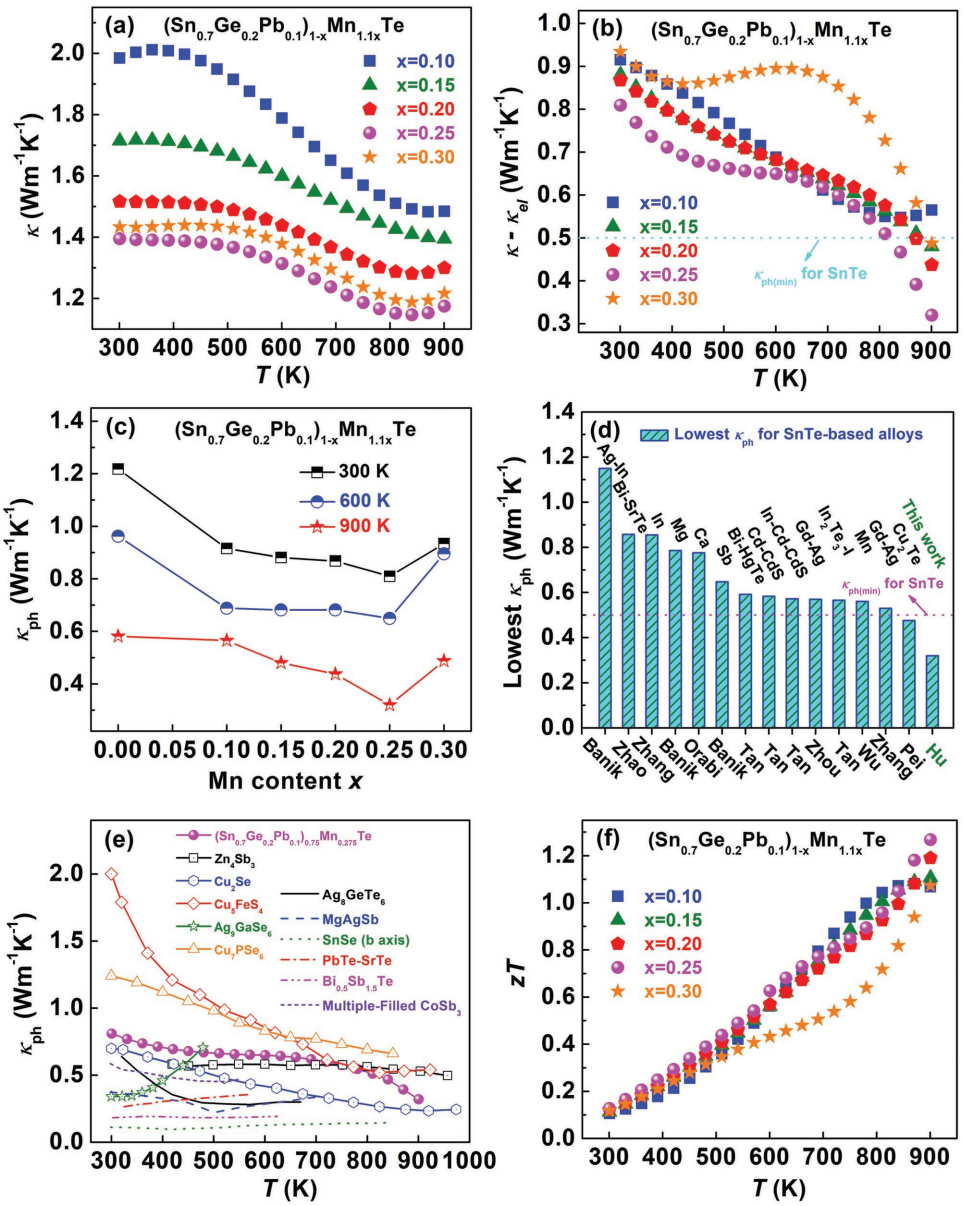

Figure 9. Temperature dependence of a) thermal conductivity, b) lattice thermal conductivity, and f) zT values for $(Sn_{0.7}Ge_{0.2}Pb_{0.1})_{1-x}Mn_{1.1x}Te$ alloys. c) Lattice thermal conductivity as a function of Mn content for $(Sn_{0.7}Ge_{0.2}Pb_{0.1})_{1-x}Mn_{1.1x}Te$ at 300, 600, and 900 K. d) The lowest lattice thermal conductivity in this work in comparison with those of other SnTe-based alloys.[15–17,19–21,24,26,28,47,48] e) Temperature-dependent lattice thermal conductivities derived in the present work and other TE materials.[6,7,29–35,49,50]

the highest zT reaches 1.27 at 900 K for the $x = 0.25$ sample, mainly due to the effective phonon scattering by the all-scale hierarchical microstructures.

2.3. Optimizing Power Factor via Tuning Sn Excess

Building on the ultralow κ_{ph} values derived in Ge–Pb–Mn-coalloyed SnTe in Section 2.2, our focus is shifted back to the PF. The approach is to reduce the hole concentrations that are otherwise too high (≈10^{21} cm^{-3}).[16] To this end, a 1–5% Sn excess was implemented in the $Sn_{0.525+y}Ge_{0.15}Pb_{0.075}Mn_{0.275}Te$ (y = 0–0.05) sample. As shown in Figure S6 (Supporting Information), the decreased σ and increased S with increasing Sn excess indicate a reduced n_H. The PF is enhanced due to the improved S at high temperatures. Despite increased κ_{ph} and κ, the $y = 0.03$ sample demonstrated the highest zT of 1.42 at 900 K (**Figure 10**a).

Figure 10b summarizes the zT improvement of SnTe-based solid solutions in the present work. The maximum zT value is higher than most SnTe-based alloys,[16,17,19–21,24,26,28,47,48,51] and close to the record zT value for $(SnTe)_{0.94}(Cu_2Te)_{0.06}$[15] (Figure 10c). The $Sn_{0.555}Ge_{0.15}Pb_{0.075}Mn_{0.275}Te$ sample exhibits the highest zT values around 800 K (Figure S7, Supporting Information). While the peak zT value is important, the average zT_{ave} value is of greater significance in applications. As shown

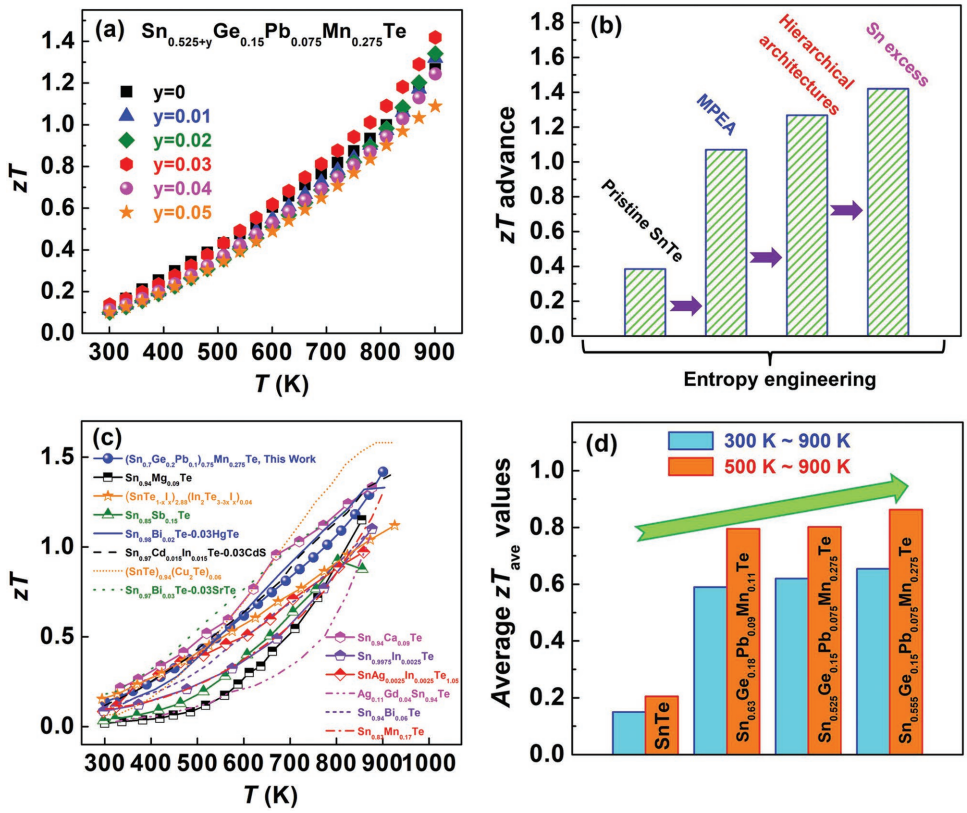

Figure 10. a) zT values as a function of temperature for $Sn_{0.525+y}Ge_{0.15}Pb_{0.075}Mn_{0.275}Te$ alloys. b) The main contributors to the zT advances and d) average zT_{ave} advances between 300–900 and 500–900 K of the SnTe-based alloys in this work. c) Temperature-dependent zT for $Sn_{0.555}Ge_{0.15}Pb_{0.075}Mn_{0.275}Te$, comparing with those of other high-zT SnTe materials.[15–17,19–21,24,26,28,47,48,51]

in Figure 10d, the average zT_{ave} of $Sn_{0.555}Ge_{0.15}Pb_{0.075}Mn_{0.275}Te$ sample is 0.66 in the range of 300–900 K and 0.87 in the range of 500–900 K. Again, considering the two motivations of the present work, the success lies in a synergy of band structure engineering and hierarchical microstructures via the MPEA procedure, a novel approach.

3. Conclusions

In the context of entropy engineering, we implemented a multi-principal-element alloying scheme to attain a delicate balance between structural order (the rock salt structure) and disorder (high entropy of mixing and microstructures) in SnTe. We observed a systematic crossover from acoustic phonon scattering to alloy scattering with increasing number of alloying elements. Owing to the core effects of high entropy alloys, the Mn solubility was significantly enhanced, the resulting all-scale hierarchical microstructures yielded a lower-than-amorphous-limit lattice thermal conductivity ≈ 0.32 W m^{-1} K^{-1} at 900 K in the simple face-centered-cubic (Sn,Ge,Pb,Mn)Te. For the first time, the intertwined line defects and strain clusters are reported in high-entropy thermoelectric materials. The multi-principal-element alloying scheme also facilitated the band convergence and increased the band effective mass, which compensated for the loss of carrier mobility and improved the power factor. Further tuning the Sn excess led to a zT of 1.42 at 900 K as well as high averaged zT_{ave} values over a wide temperature range in $Sn_{0.555}Ge_{0.15}Pb_{0.075}Mn_{0.275}Te$.

The results reported herein will inspire more theoretical works on the high-entropy thermoelectric alloys, enrich our understanding of defect engineering, and contribute to an emerging paradigm of "high entropy thermoelectrics." In particular, a new theme "in what order to alloy" emerges on top of the traditional themes "what to alloy" and "how much to alloy" that are common in multielement doping study. The cocktail effects make a high-entropy alloy beyond a simple sum (average) of the low-entropy components, promising unprecedented opportunities in those semiconductors with high crystal lattice symmetry.

4. Experimental Section

Synthesis of Starting Materials: High-purity Sn (99.999%), Pb (99.999%), Ge (99.999%), Mn (99.99%), and Te (99.999%) were used to synthesize the following samples: SnTe, $Sn_{0.8}Ge_{0.2}Te$, $Sn_{0.7}Ge_{0.2}Pb_{0.1}Te$, $(Sn_{0.7}Ge_{0.2}Pb_{0.1})_{1-x}Mn_{1.1x}Te$ with x = 0.1, 0.15, 0.2, 0.25, and 0.3; and $Sn_{0.525+y}Ge_{0.15}Pb_{0.075}Mn_{0.275}Te$ with y = 0.01, 0.02, 0.03, 0.04, and 0.05. Appropriate amounts of Sn, Pb, Ge, Mn, and Te were weighed, mixed, and sealed in evacuated silica tubes. The admixtures were melted at 1323 K for 10 h, quenched in cold water, ground into fine powders, and then consolidated into pellets by spark plasma sintering at 873 K for 5 min under an axial pressure of 50 MPa. The relative densities of all the samples were >95% of the theoretical ones.

X-Ray Diffraction and Electron Microscopy Study: Phase structures of the as-synthesized samples were checked by XRD using a Bruker D8 Advance SS/18 kW diffractometer with the Cu Kα radiation. The lattice parameters were derived from the Rietveld refinements using the Topas 3.1 software. The microstructures were inspected by SEM (Hitachi SU-70, Japan) and the compositions were measured by EDS. The samples for STEM and TEM (JEOL ARM200F equipped with cold field emission gun, ASCOR probe corrector and Oxford X-Max 100TLE SDD EDS) were prepared by the conventional standard methods including cutting, grinding, dimpling, polishing, and Ar-ion milling on a liquid nitrogen cooling stage.

Transport Property Characterization: The Hall coefficient R_H was measured on a Quantum Design physical property measurement system (PPMS) instrument with the magnetic field sweeping between ±5 T at room temperature. The effective hole concentration n_H and effective Hall mobility μ_H were calculated by the relations: $n_H = 1/eR_H$ and $\mu_H = \sigma R_H$, respectively. The uncertainty of R_H measurements was ±5%. The Seebeck coefficient S and the electrical conductivity σ were simultaneously measured on a ZEM-2 apparatus (Ulvac-Riko, Japan) in a helium atmosphere. The uncertainty of σ and S measurements was ±3%. The thermal diffusivity D was determined on a Netzsch LFA 457 laser flash apparatus. The isobaric heat capacity C_p was measured by the Netzsch DSC 404C, and the bulk density ρ was estimated by sample dimension and mass. The uncertainties of D and C_p measurements were ±3% and ±5%, respectively. The thermal conductivity κ was calculated using the relation: $\kappa = D\rho C_p$.

Electronic Band Structure Calculations: DFT band structure calculations were performed using the Perdew–Burke–Ernzerhof (PBE) functional as implemented in the Vienna Ab initio Simulation Package (VASP). A plane wave energy cutoff of 400 eV was applied, and the energy convergence criterion for charge self-consistency was 10^{-5} eV. A Monkhorst–Pack k-point mesh of $3 \times 3 \times 3$ was applied for the self-consistent calculations of the $3 \times 3 \times 3$ $Sn_{27}Te_{27}$ supercell. The $Sn_{22}Ge_5Te_{27}$, $Sn_{19}Ge_5Pb_3Te_{27}$, and $Sn_{18}Ge_5Pb_2Mn_2Te_{27}$ supercells were studied to probe the effects of Ge alloying, Ge–Pb coalloying, and Ge–Pb–Mn coalloying on the electronic band structure. These compositions are close to the nominal compositions of samples in experiments. The anti-ferromagnetic ground state in the Mn-doped system was found to be energetically favorable. All the systems were fully relaxed before the band structure calculations, and the spin–orbit coupling (SOC) effects were included.

Supporting Information

Supporting Information is available from the Wiley Online Library or from the author.

Acknowledgements

The work was supported by the National Natural Science Foundation of China (Grant Nos. 51571144, 51701126, and 11504239), the National Postdoctoral Program for Innovative Talents of China (Grant No. BX201600110), the China Postdoctoral Science Foundation (Grant No. 2016M602515), and the Shenzhen Science and Technology Research Grant (No. JCYJ20150827155136104). J.H. would like to acknowledge the financial support from the NSF DMR1307740. S.J.P. would like to acknowledge funding from the National University of Singapore. The authors would like to thank Dr. C. Chen and Prof. Q. Zhang from the Harbin Institute of Technology for thermal conductivity measurement and Daniel Fox for proofreading the paper.

Conflict of Interest

The authors declare no conflict of interest.

Keywords

band convergence, entropy engineering, microstructures, SnTe, thermoelectric

Received: July 10, 2018
Revised: August 3, 2018
Published online: September 10, 2018

[1] a) J. He, T. M. Tritt, *Science* **2017**, *357*, eaak9997; b) T. J. Zhu, Y. T. Liu, C. G. Fu, J. P. Heremans, J. G. Snyder, X. B. Zhao, *Adv. Mater.* **2017**, *29*, 1605884; c) J. H. Yang, H. L. Yip, A. K. Y. Jen, *Adv. Energy Mater.* **2013**, *3*, 549.

[2] G. A. Slack, in *CRC Handbook of Thermoelectrics* (Ed: D. M. Rowe), CRC Press, Boca Raton **1995**, p. 407.

[3] a) Y. Z. Pei, X. Shi, A. LaLonde, H. Wang, L. Chen, G. J. Snyder, *Nature* **2011**, *473*, 66; b) Y. Z. Pei, A. D. LaLonde, N. A. Heinz, G. J. Snyder, *Adv. Energy Mater.* **2012**, *2*, 670; c) Y. Z. Pei, A. F. May, G. J. Snyder, *Adv. Energy Mater.* **2011**, *1*, 291.

[4] J. P. Heremans, V. Jovovic, E. S. Toberer, A. Saramat, K. Kurosaki, A. Charoenphakdee, S. Yamanaka, G. J. Snyder, *Science* **2008**, *321*, 554.

[5] a) L. P. Hu, H. J. Wu, T. J. Zhu, C. G. Fu, J. Q. He, P. J. Ying, X. B. Zhao, *Adv. Energy Mater.* **2015**, *5*, 1500411; b) L. P. Hu, T. J. Zhu, X. H. Liu, X. B. Zhao, *Adv. Funct. Mater.* **2014**, *24*, 5211; c) L. P. Hu, Y. Zhang, H. J. Wu, Y. M. Liu, J. Q. Li, J. He, W. Q. Ao, F. S. Liu, S. J. Pennycook, X. R. Zeng, *Adv. Funct. Mater.* **2018**, *28*, 1803617.

[6] K. Biswas, J. He, I. D. Blum, C. I. Wu, T. P. Hogan, D. N. Seidman, V. P. Dravid, M. G. Kanatzidis, *Nature* **2012**, *489*, 414.

[7] X. Shi, J. Yang, J. R. Salvador, M. F Chi, J. Y. Cho, H. Wang, S. Q. Bai, J. H. Yang, W. Q. Zhang, L. D. Chen, *J. Am. Chem. Soc.* **2011**, *133*, 7837.

[8] a) Y. Zhang, T. T. Zuo, Z. Tang, M. C. Gao, K. A. Dahmen, P. K. Liaw, Z. P. Lu, *Prog. Mater. Sci.* **2014**, *61*, 1; b) O. N. Senkov, J. D. Miller, D. B. Miracle, C. Woodward, *Nat. Commun.* **2015**, *6*, 6529.

[9] R. H. Liu, H. Y. Chen, K. P. Zhao, Y. T. Qin, B. B. Jiang, T. S. Zhang, G. Sha, X. Shi, C. Uher, W. Q. Zhang, L. D. Chen, *Adv. Mater.* **2017**, *29*, 1702712.

[10] S. Shafeie, S. Guo, Q. Hu, H. Fahlquist, P. Erhart, A. Palmqvist, *J. Appl. Phys.* **2015**, *118*, 184905.

[11] Z. Fan, H. Wang, Y. Wu, X. J. Liu, Z. P. Lu, *Mater. Res. Lett.* **2017**, *5*, 187.

[12] Z. Fan, H. Wang, Y. Wu, X. J. Liu, Z. P. Lu, *RSC Adv.* **2016**, *6*, 52164.

[13] a) R. Moshwan, L. Yang, J. Zou, Z. G. Chen, *Adv. Funct. Mater.* **2017**, *27*, 1703278; b) W. Li, Y. X. Wu, S. Q. Lin, Z. W. Chen, J. Li, X. Y. Zhang, L. L. Zheng, Y. Z. Pei, *ACS Energy Lett.* **2017**, *2*, 2349; c) Y. Chen, M. D. Nielsen, Y. B. Cao, T. J. Zhu, X. B. Zhao, J. P. Heremans, *Adv. Energy Mater.* **2012**, *2*, 58.

[14] L. V. Yashina, V. Leute, V. I. Shtanov, H. M. Schmidtke, V. S. Neudachina, *J. Appl. Phys.* **2006**, *413*, 133.

[15] a) W. Li, L. L. Zheng, B. H. Ge, S. Q Lin, X. Y. Zhang, Z. W. Chen, Y. J. Chang, Y. Z. Pei, *Adv. Mater.* **2017**, *29*, 1605887; b) W. Li, Z. W. Chen, S. Q. Lin, Y. J. Chang, B. H. Ge, Y. Chen, Y. Z. Pei, *J. Materiomics* **2015**, *1*, 307; c) J. Tang, B. Gao, S. Q. Lin, J. Li, Z. W. Chen, F. Xiong, W. Li, Y. Chen, Y. Z. Pei, *Adv. Funct. Mater.* **2018**, *28*, 1803586.

[16] a) G. J. Tan, F. Shi, J. W. Doak, H. Sun, L. D. Zhao, P. Wang, C. Uher, C. Wolverton, V. P. Dravid, M. G. Kanatzidis, *Energy Environ. Sci.* **2015**, *8*, 267; b) G. J. Tan, L. D. Zhao, F. Shi, J. W. Doak, S. H. Lo, H. Sun, C. Wolverton, V. P. Dravid, C. Uher, M. G. Kanatzidis, *J. Am. Chem. Soc.* **2014**, *136*, 7006; c) G. J. Tan, F. Shi, S. Hao, H. Chi, T. P. Bailey, L. D. Zhao, C. Uher, C. Wolverton, V. P. Dravid,

M. G. Kanatzidis, *J. Am. Chem. Soc.* **2015**, *137*, 11507; d) M. K. Han, X. Y. Zhou, C. Uher, S. J. Kim, M. G. Kanatzidis, *Adv. Energy Mater.* **2012**, *2*, 1218.

[17] a) H. J. Wu, C. Chang, D. Feng, Y. Xiao, X. Zhang, Y. Pei, L. Zheng, D. Wu, S. K. Gong, Y. Chen, J. Q. He, M. G. Kanatzidis, L. D. Zhao, *Energy Environ. Sci.* **2015**, *8*, 3298; b) N. Wang, D. West, J. W. Liu, J. Li, Q. M. Yan, B. Gu, S. B. Zhang, W. H. Duan, *Phys. Rev. B* **2014**, *89*, 045142; c) S. Acharya, S. Anwar, T. Mori, A. Soni, *J. Mater. Chem. C* **2018**, *6*, 6489.

[18] S. M. Li, J. Q. Li, L. Yang, F. S. Liu, W. Q. Ao, Y. Li, *Mater. Des.* **2016**, *108*, 51.

[19] a) Q. Zhang, B. Liao, Y. Lan, K. Lukas, W. Liu, K. Esfarjani, C. Opeil, D. Broido, G. Chen, Z. F. Ren, *Proc. Natl. Acad. Sci. USA* **2013**, *110*, 13261; b) G. J. Tan, W. G. Zeier, F. Shi, P. Wang, G. J. Snyder, V. P. Dravid, M. G. Kanatzidis, *Chem. Mater.* **2015**, *27*, 7801.

[20] R. A. R. A. Orabi, N. A. Mecholsky, J. Hwang, W. Kim, J. S. Rhyee, D. Wee, M. Fornari, *Chem. Mater.* **2015**, *28*, 376.

[21] a) A. Banik, U. S. Shenoy, S. Anand, U. V. Waghmare, K. Biswas, *Chem. Mater.* **2015**, *27*, 581; b) A. Banik, K. Biswas, *J. Solid State Chem.* **2016**, *242*, 43.

[22] J. He, X. Tan, J. Xu, G. Liu, H. Shao, Y. Fu, X. Wang, Z. Liu, J. Xu, H. Jiang, J. Jiang, *J. Mater. Chem. A* **2015**, *3*, 19974.

[23] H. C. Wang, J. Hwang, C. Zhang, T. Wang, W. B. Su, H. Kim, J. Kim, J. Zhai, X. Wang, H. Park, W. Kim, C. L. Wang, *J. Mater. Chem. A* **2017**, *5*, 14165.

[24] A. Banik, U. S. Shenoy, S. Saha, U. V. Waghmare, K. Biswas, *J. Am. Chem. Soc.* **2016**, *138*, 13068.

[25] D. K. Bhat, U. S. Shenoy, *J. Phys. Chem. C* **2017**, *121*, 7123.

[26] G. J. Tan, F. Shi, S. Hao, H. Chi, L. D. Zhao, C. Uher, C. Wolverton, V. P. Dravid, M. G. Kanatzidis, *J. Am. Chem. Soc.* **2015**, *137*, 5100.

[27] L. Wang, X. J. Tan, G. Q. Liu, J. T. Xu, H. Z. Shao, B. Yu, H. C. Jiang, S. Yue, J. Jiang, *ACS Energy Lett.* **2017**, *2*, 1203.

[28] a) A. Banik, B. Vishal, S. Perumal, R. Datta, K. Biswas, *Energy Environ. Sci.* **2016**, *9*, 2011; b) A. Banik, K. Biswas, *J. Mater. Chem. A* **2014**, *2*, 9620.

[29] G. Snyder, M. Christensen, E. Nishibori, T. Caillat, B. Iversen, *Nat. Mater.* **2004**, *3*, 458.

[30] H. Liu, X. Shi, F. Xu, L. Zhang, W. Zhang, L. Chen, Q. Li, C. Uher, T. Day, G. J. Snyder, *Nat. Mater.* **2012**, *11*, 422.

[31] L. D. Zhao, S. H. Lo, Y. Zhang, H. Sun, G. Tan, C. Uher, C. Wolverton, V. P. Dravid, M. G. Kanatzidis, *Nature* **2014**, *508*, 373.

[32] T. J. Zhu, S. N. Zhang, S. H. Yang, X. B. Zhao, *Phys. Status Solidi RRL* **2010**, *4*, 317.

[33] S. Q. Lin, W. Li, S. S. Li, X. Y. Zhang, Z. W. Chen, Y. D. Xu, Y. Chen, Y. Z. Pei, *Joule* **2017**, *1*, 1.

[34] K. S. Weldert, W. G. Zeier, T. W. Day, M. Panthofer, G. J. Snyder, W. Tremel, *J. Am. Chem. Soc.* **2014**, *136*, 12035.

[35] D. Li, H. Zhao, S. Li, B. Wei, J. Shuai, C. Shi, X. Xi, P. Sun, S. Meng, L. Gu, Z. F. Lin, X. L. Chen, *Adv. Funct. Mater.* **2015**, *25*, 6478.

[36] V. P Vedeneev, S. P. Krivoruchko, E. P. Sabo, *Semiconductors* **1998**, *32*, 241.

[37] J. Q. Li, S. Huang, Z. P. Chen, Y. Li, S. H. Song, F. S. Liu, W. Q. Ao, *Phys. Chem. Chem. Phys.* **2017**, *19*, 28749.

[38] M. Zhou, Z. M. Gibbs, H. Wang, Y. M. Han, C. N. Xin, L. F. Li, G. J. Snyder, *Phys. Chem. Chem. Phys.* **2014**, *16*, 20741.

[39] T. H. Hsieh, H. Lin, J. W. Liu, W. H. Duan, A. Bansil, L. Fu, *Nat. Commun.* **2012**, *3*, 982.

[40] L. M. Rogers, *J. Appl. Phys.* **1968**, *2*, 845.

[41] H. S. Kim, Z. M. Gibbs, Y. Tang, H. Wang, G. J. Snyder, *APL Mater.* **2015**, *3*, 041506.

[42] S. Perumal, S. Roychowdhury, K. Biswas, *J. Mater. Chem. C* **2016**, *4*, 7520.

[43] S. Roychowdhury, U. S. Shenoy, U. V. Waghmareb, K. Biswas, *J. Mater. Chem. C* **2017**, *5*, 5737.

[44] H. J. Wu, F. S. Zheng, D. Wu, Z. H. Ge, X. Y. Liu, J. Q. He, *Nano Energy* **2015**, *13*, 626.

[45] H. J. Wu, L. D. Zhao, F. S. Zheng, D. Wu, Y. L. Pei, X. Tong, M. G. Kanatzidis, J. Q. He, *Nat. Commun.* **2014**, *5*, 4515.

[46] L. D. Zhao, H. J. Wu, S. Q. Hao, C. I. Wu, X. Y. Zhou, K. Biswas, J. Q. He, T. P. Hogan, C. Uher, C. Wolverton, V. P. Dravid, M. G. Kanatzidis, *Energy Environ. Sci.* **2013**, *6*, 3346.

[47] a) X. Zhang, D. Y. Wang, H. J. Wu, M. J. Yin, Y. L. Pei, S. K. Gong, L. Huang, S. J. Pennycook, J. Q. He, L. Dong Zhao, *Energy Environ. Sci.* **2017**, *10*, 2420; b) L. D. Zhao, X. Zhang, H. J. Wu, G. J. Tan, Y. L. Pei, Y. Xiao, C. Chang, D. Wu, H. Chi, L. Zheng, S. K. Gong, C. Uher, J. Q. He, M. G. Kanatzidis, *J. Am. Chem. Soc.* **2016**, *138*, 2366.

[48] L. J. Zhang, J. L. Wang, Z. X. Cheng, Q. Sun, Z. Li, S. X. Dou, *J. Mater. Chem. A* **2016**, *4*, 7936.

[49] S. I. Kim, K. H. Lee, H. A. Mun, H. S. Kim, S. W. Hwang, J. W. Roh, D. J. Yang, W. H. Shin, X. S. Li, Y. H. Lee, *Science* **2015**, *348*, 109.

[50] P. F. Qiu, T. S. Zhang, Y. T. Qiu, X. Shi, L. D. Chen, *Energy Environ. Sci.* **2014**, *7*, 4000.

[51] Z. W. Zhou, J. Y. Yang, Q. H. Jiang, Y. B. Luo, D. Zhang, Y. Y. Ren, X. He, J. W. Xin, *J. Mater. Chem. A* **2016**, *4*, 13171.